# Faster Diffusion of Oxygen along Dislocations in (La,Sr)MnO$_{3+\delta}$ Is a Space-Charge Phenomenon

*Jacqueline M. Börgers, Joe Kler, Ke Ran, Elizabeth Larenz, Thomas E. Weirich, Regina Dittmann, Roger A. De Souza* *

J. M. Börgers
Institute of Physical Chemistry, RWTH Aachen University, 52056 Aachen, Germany
Peter Gruenberg Institute 7, Forschungszentrum Juelich GmbH, 52425 Juelich, Germany
J. Kler
Institute of Physical Chemistry, RWTH Aachen University, 52056 Aachen, Germany
Dr. K. Ran
Central Facility for Electron Microscopy, RWTH Aachen University, 52074 Aachen, Germany
E. Larenz
Institute of Physical Chemistry, RWTH Aachen University, 52056 Aachen, Germany
Prof. Dr. T. E. Weirich
Central Facility for Electron Microscopy, RWTH Aachen University, 52074 Aachen, Germany
Prof. Dr. R. Dittmann
Peter Gruenberg Institute 7, Forschungszentrum Juelich GmbH, 52425 Juelich, Germany
Prof. Dr. R. A. De Souza
Institute of Physical Chemistry, RWTH Aachen University, 52056 Aachen, Germany
Email Address: desouza@pc.rwth-aachen.de

Keywords: *oxygen diffusion, SIMS, manganite perovskite, dislocations, molecular dynamics*

In displaying accelerated oxygen diffusion along extended defects, (La,Sr)MnO$_{3+\delta}$ is an atypical acceptor-doped perovskite-type oxide. In this study, $^{18}$O/$^{16}$O diffusion experiments on epitaxial thin films of La$_{0.8}$Sr$_{0.2}$MnO$_{3+\delta}$ and molecular dynamics (MD) simulations were combined to elucidate the origin of this phenomenon for dislocations: Does diffusion occur along dislocation cores or space-charge tubes? Transmission electron microscopy (TEM) studies of the films revealed dislocations extending from the surface. $^{18}$O penetration profiles measured by secondary ion mass spectrometry (SIMS) indicated (slow) bulk diffusion and faster diffusion along dislocations. Oxygen tracer diffusivities obtained for temperatures $873 \leq T$ [K] $\leq 973$ were over two orders of magnitude higher for dislocations than for the bulk. The activation enthalpy of oxygen diffusion along dislocations, of (2.95 ± 0.21) eV, is surprisingly high relative to that for bulk diffusion, (2.67 ± 0.13) eV. This result militates against fast diffusion along dislocation cores. MD simulations confirmed no accelerated migration of oxide ions along dislocation cores. Faster diffusion of oxygen along dislocations in La$_{0.8}$Sr$_{0.2}$MnO$_{3+\delta}$ is thus concluded to occur within space-charge tubes in which oxygen vacancies are strongly accumulated. Reasons for and the consequences of space-charge zones at extended defects in manganite perovskites are discussed.

## 1 Introduction

Introducing extended defects, such as dislocations or grain boundaries, into a crystalline solid constitutes an interesting possibility for accelerating ion transport beyond the confines of compositional optimization. For the best ion conductors, however, this possibility seems remote:[1,2] the transport of highly mobile ions is evidently diminished at extended defects on account of the perturbed crystal structure. In contrast, poor ion conductors appear to benefit from such structural perturbations. A promising avenue of research, therefore, is the introduction of extended defects into poor ion conductors.

On this basis, one system of particular interest is the perovskite-type oxide (La,Sr)MnO$_{3+\delta}$ (LSMO). In contrast to other strontium-substituted lanthanum transition-metal perovskites [e.g. (La,Sr)CoO$_3$[3,4]], LSMO exhibits (a) rather slow oxygen diffusion in the bulk[3–10] and (b) faster oxygen diffusion along extended defects, such as grain boundaries[8,10–13] and dislocations,[14] than in the bulk. The low rates of bulk diffusion are now known to arise from a combination of two factors: a very low concentration of oxygen vacancies (oxygen-excess LSMO having a high concentration of cation vacancies that drastically lowers the concentration of oxygen vacancies through a Schottky equilibrium[15–20]); and a low diffusivity of oxygen vacancies (cation vacancies strongly retarding oxygen-vacancy diffusion[21]). The reasons for

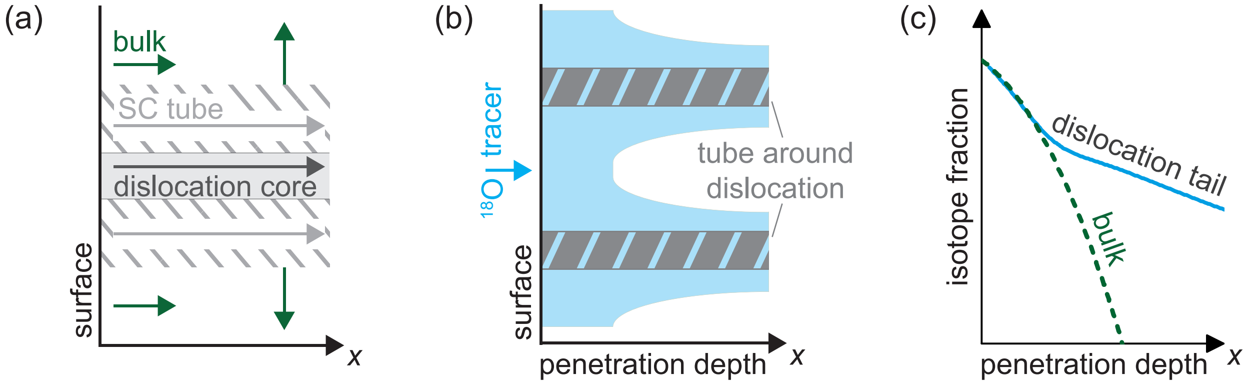

Figure 1: Accelerated diffusion along a dislocation with attendant space-charge tube in an ionic solid. (a) Fast diffusion along the space-charge tube (bright grey arrow) relative to that in the bulk (green arrows) may occur in addition to, or instead of, diffusion along the dislocation core (dark grey arrow). (b) The diffusion front has the same form regardless of whether fast diffusion occurs along the core, the space-charge tube, or some combination thereof. (c) Diffusion profile obtained from the two-dimensional distribution shown in (b), showing the first feature arising from bulk diffusion and the second feature, the dislocation tail, arising from fast diffusion along the dislocation and slow bulk diffusion out of it.

fast oxygen diffusion along extended defects in LSMO are not clear,[21–23] however; such knowledge is essential for tuning oxide-ion transport in LSMO for application as a cathode material in solid oxide fuel cells (SOFC)[24–27] or as the active material in memristive devices.[28–34]

In ionic solids, there are two possibilities to explain the phenomenon of fast diffusion along dislocations[23] [see Figure 1 (a)]: (i) diffusion along the dislocation core is faster than in the bulk on account of the activation barrier for ion migration being lower in the core than in the bulk, as is the case in metals; (ii) the concentration of the defects responsible for diffusion is strongly enhanced in a space-charge tube surrounding the dislocation.[23,35,36] For LSMO, literature provides at present an unclear picture. On the one hand, Navickas et al.[14], in their experimental study, proposed diffusion along the core. Atomistic simulations of the closely related perovskite $SrTiO_3$ show, however, that oxygen-vacancy migration along dislocation cores is hindered.[1,37,38] On the other hand, one may be tempted to argue that space-charge tubes are negligible in LSMO, owing to the very high concentration of electronic defects. This argument rests on LSMO being treated as a dilute solution and on invoking dilute-solution concepts, such as the Debye length. LSMO, however, is a concentrated solid solution, for which defect interactions need to be taken into account in a suitable manner, for example, within Poisson–Cahn theory.[39,40,42] In other words, there are arguments both for and against both possibilities, and a detailed examination is therefore warranted.

In this study, based on a careful choice of methods and system, we examined the diffusion of oxygen along dislocations in $La_{0.8}Sr_{0.2}MnO_{3+\delta}$. As the main experimental method, we employed oxygen isotope exchange ($^{18}O/^{16}O$) experiments with profile determination by means of time-of-flight subsequent secondary ion mass spectrometry (ToF-SIMS). The method is well established[3,41,43–46], and has in the present case the particular benefit of providing unambiguous diffusion data. An isotope profile in the solid, consisting of two features, each displaying a characteristic mathematical form[47] constitutes unambiguous evidence of slower bulk diffusion and faster diffusion along dislocations. One problem, though, is that a single diffusion profile cannot differentiate between the two possibilities of diffusion along the core and along the space-charge tube [see Figure 1 (b) and (c)]. Here, we demonstrate that the origin of fast oxygen diffusion along dislocations in LSMO can be clarified by obtaining experimental data as a function of temperature and by performing molecular dynamics (MD) simulations of oxygen diffusion to aid the interpreta-

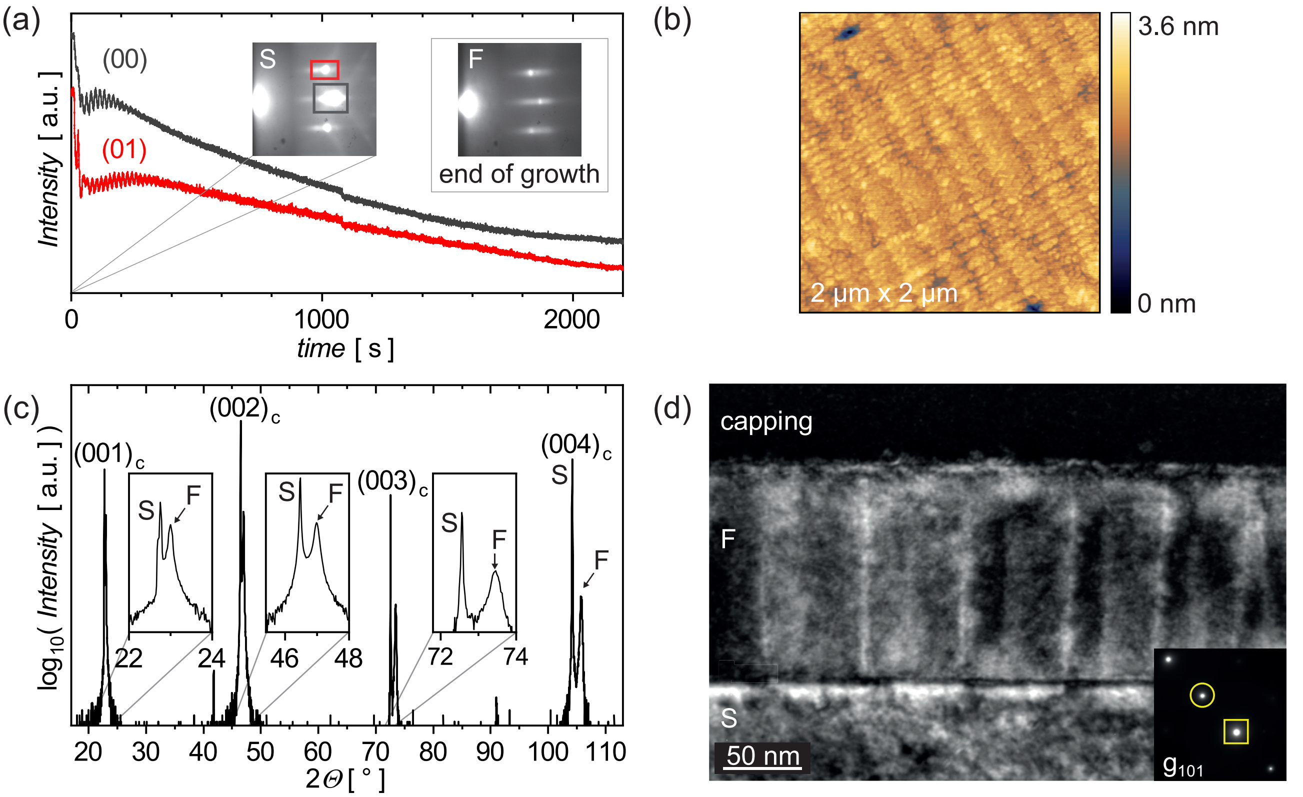

Figure 2: Thin film characterization of a $La_{0.8}Sr_{0.2}MnO_3$ film (marked as F) on a $SrTiO_3$ substrate (marked as S). (a) In-situ recorded RHEED intensity oscillations for thin film growth, that were integrated from (00)/(01) reflection (framed in the reflection pattern gray/red respectively). Reflection patterns are shown for the intial substrate and for the finally grown thin film of 130 nm thickness (deposition completed after 6400 s). b) Surface morphology of the grown thin film obtained by AFM for a 2 $\mu$m × 2 $\mu$m wide area. (c) $2\Theta - \Theta$-scan along $(00L)_c$ obtained by XRD after oxidative treatment: due to lattice mismatch, $La_{0.8}Sr_{0.2}MnO_3$ film peaks are shifted to higher angles next to the $SrTiO_3$ peaks; the absence of further peaks confirms epitaxial growth. (The resulting out-of-plane lattice constant of $La_{0.8}Sr_{0.2}MnO_3$ is 3.86 nm.) (d) Weak-beam dark-field (WBDF) image: in the $La_{0.8}Sr_{0.2}MnO_3$ film, dislocations appear bright on a dark background. Note that the image is a 2D projection and hence that the dislocations are not necessary equidistant. The inset shows the diffraction condition, where the transmitted beam is framed with a circle and the excited diffraction spot g=(101) is framed with a square.

tion of experimental results. Such simulations permit atomic scale insights into a dislocation-containing system at finite temperatures.

As a suitable system, we chose epitaxial $La_{0.8}Sr_{0.2}MnO_3$ (with $a_{\mathrm{pc,lit}} = 3.883$ Å[48,49]) on $SrTiO_3$ (STO) ($a = 3.905$ Å). Specifically we made use of the mismatch ($-0.56\%$) between film and substrate that, upon relaxation of the tensile strain, generates edge dislocations perpendicular to the surface[50,51] (rather than plastically deforming samples macroscopically[52,53] or microscopically[54]).

## 2 Results

We begin by confirming that the films grown by pulsed laser deposition (PLD) are epitaxial, under tensile strain, and smooth. Reflection high-energy electron diffraction (RHEED), performed during film growth, indicated a layer-by-layer growth mode, as shown in Figure 2(a). The grown thin films of 130 nm thickness displayed in addition a smooth surface morphology, according to the RHEED pattern recorded after growth and according to the AFM analysis [see Figure 2(b)]. An r.m.s. surface roughness of approximately 260 pm was achieved. Figure 2(c) shows a $2\Theta - \Theta$ scan along $(00L)_c$ (referring to cubic STO) obtained by X-ray diffraction (XRD) after oxidative treatment; it indicates (i) that the thin films are epitaxial and (ii) that after the treatment they are not fully strained but at least partial relaxed.

A weak-beam dark-field (WBDF) image of the system after oxidative treatment is shown in Figure 2(d),

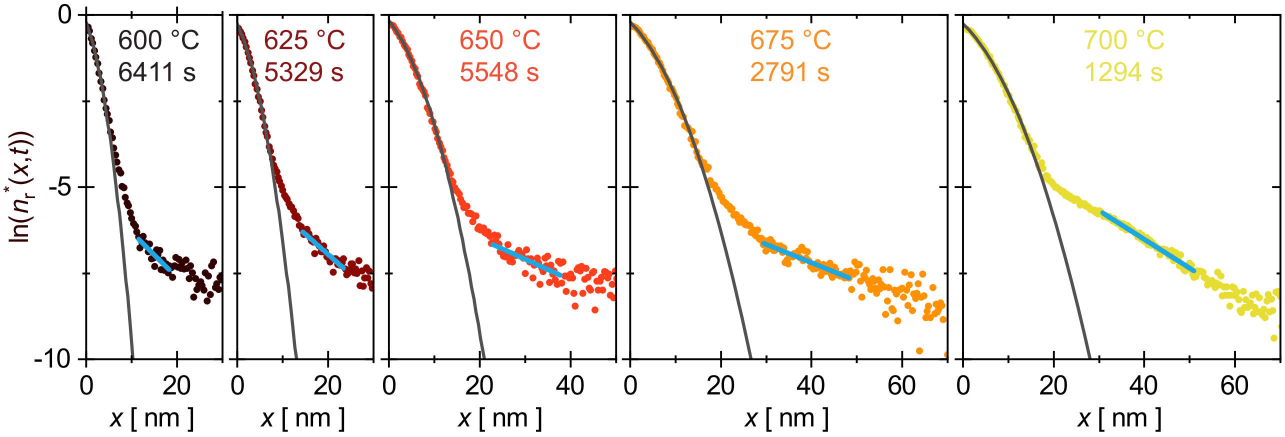

Figure 3: $^{18}$O diffusion profiles obtained for $\mathrm{La_{0.8}Sr_{0.2}MnO_{3+\delta}}$ by means of ToF-SIMS analysis shown as normalized isotope fraction $n_\mathrm{r}^*(x,t)$ versus depth $x$. At all temperature examined, two features are seen in the diffusion profiles (see Figure 1), and the penetration depth does not exceed the thickness of the thin film. Also plotted are the fits to Equation (1) for the bulk (grey lines) and to Equation (2) for the dislocation tails (blue lines).

with the inset (lower right) showing the diffraction condition. The WBDF image clearly indicates the presence of dislocations reaching into the film from the surface, mainly parallel to the (100) plane. Since the lines' intensity is homogeneous along their length, this strongly suggests that their line vector is $\mathbf{l} = [001]$. The Burgers vector of these dislocations, calculated according to $\mathbf{g} \cdot \mathbf{b} = 0$, is $\mathbf{b} = [010]$. WBDF images obtained for different parts of the film indicated far fewer dislocations, that is, the distribution of dislocations is not homogeneous over the film, making it difficult to determine a characteristic dislocation density. The zone-axis diffraction patterns (SI, Figure S1) allow us to exclude the possibility of the observed extended defects being domain walls, i.e., they are also consistent with the presence of dislocations.

It was important to grow relatively thick films with low surface roughness, in order to enhance the quality of the diffusion data. Short bulk diffusion profiles obtained by SIMS may well be distorted by surface roughness,[55] and dislocation tails may yield imprecise data if the tail is flattened by the diffusion front reaching the end of the film.

Several ToF-SIMS measurements were carried out on each isotope-exchanged sample. An example profile for each investigated temperature is plotted in Figure 3 as normalized isotope fraction against depth $x$ (with all obtained profiles shown in Figure S2, S3, S4). All measured profiles displayed two features, as expected [cf. Figure 1 (c)], and the forms of these features strongly suggest that the first feature is due to bulk diffusion and the second, to fast diffusion along the dislocation and slow bulk diffusion out of it. Indeed, the first feature can be described quantitatively in all cases with the appropriate solution of the diffusion equation (diffusion into a homogeneous medium from a large volume of isotope with surface-limited incorporation),

$$n_\mathrm{r}^*(x,t) = \mathrm{erfc}\left[\frac{x}{2\sqrt{D_\mathrm{O}^{*,\mathrm{b}}t}}\right] - \left[\exp\left(\frac{k_\mathrm{O}^* x}{D_\mathrm{O}^{*,\mathrm{b}}} + \frac{{k_\mathrm{O}^*}^2 t}{D_\mathrm{O}^{*,\mathrm{b}}}\right) \times \mathrm{erfc}\left(\frac{x}{2\sqrt{D_\mathrm{O}^{*,\mathrm{b}}t}} + k_\mathrm{O}^*\sqrt{\frac{t}{D_\mathrm{O}^{*,\mathrm{b}}}}\right)\right], \tag{1}$$

to yield bulk diffusion coefficients $D_\mathrm{O}^{*,\mathrm{b}}$ and surface exchange coefficients $k_\mathrm{O}^*$; while the second feature shows the expected mathematical form[47] of $\ln n_\mathrm{r}^* \propto x$. We determined the characteristic slope

$$Z_\mathrm{dis} = \frac{\partial \ln n_\mathrm{r}^*(x,t)}{\partial x}, \tag{2}$$

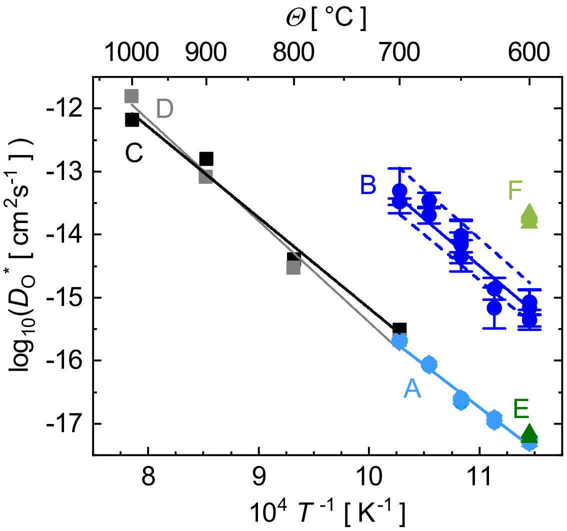

Figure 4: Oxygen tracer diffusion coefficients $D_{\mathrm{O}}^{*}$ obtained for $\mathrm{La_{0.8}Sr_{0.2}MnO_{3+\delta}}$ versus inverse temperature $T^{-1}$ : A, bulk diffusion (thin films, this study); B, dislocation diffusion (thin films, this study); C, bulk diffusion (ceramics, by De Souza et al.[8]); D, bulk diffusion (single grains in a ceramic, by Fearn et al.[9]); E, bulk diffusion (thin film, by Navickas et al.[14]); F, dislocation diffusion (thin film, by Navickas et al.[14]). The dashed lines for dataset B indicate that the values obtained for $D_{\mathrm{O}}^{*,\mathrm{dis}}$ depend on the pipe radius $r$ assumed in the analysis (see text).

over the range $6 \leq \eta \leq 10$ (where $\eta = x/\sqrt{D_{\mathrm{O}}^{*,\mathrm{b}} t}$). This range of $\eta$ was used by Chung and Wuensch[56] in their analysis of fast grain-boundary diffusion, as it starts beyond the extension of the bulk diffusion profile ($\eta < 4$) but often remains above the background-noise level. We used this range here for these reasons, and also so that it is evident over which lengths $Z_{\mathrm{dis}}$ is determined.

According to the standard treatment from Le Claire and Rabinovitch[47], which assumes fast diffusion occurring perpendicular to the surface along tubes of radius $r$, the tracer diffusion coefficient of oxygen along the dislocation is obtained from $Z_{\mathrm{dis}}$ with

$$D_{\mathrm{O}}^{*,\mathrm{dis}} = \frac{A^2 D_{\mathrm{O}}^{*,\mathrm{b}}}{\left(Z_{\mathrm{dis}}\right)^2 r^2}, \tag{3}$$

where $\alpha = r/\sqrt{D_{\mathrm{O}}^{*,\mathrm{b}} t}$ and $A = f(\alpha)$ was taken from Le Claire and Rabinovitch[47]. Obtaining $D_{\mathrm{O}}^{*,\mathrm{dis}}$ requires therefore $r$ to be specified, but this quantity depends on which mechanism is operative (core diffusion versus space-charge tube diffusion) and is thus unknown a priori. Consequently, we took three different values, $r$ [nm] $= \{0.5, 1.0, 1.5\}$, and obtained values of $D_{\mathrm{O}}^{*,\mathrm{dis}}$ accordingly. All oxygen tracer diffusion coefficients obtained in this study are shown in Figure 4, together with literature data. At a given temperature, $D_{\mathrm{O}}^{*,\mathrm{dis}}$ is higher than $D_{\mathrm{O}}^{*,\mathrm{b}}$ by just over two orders of magnitude. Decreasing $r$ from 1.0 nm to 0.5 nm leads to an increase in $D_{\mathrm{O}}^{*,\mathrm{dis}}$ by a factor of ca. 3, while increasing $r$ from 1.0 nm to 1.5 nm decreases $D_{\mathrm{O}}^{*,\mathrm{dis}}$ by a factor of 0.6. The enthalpies of oxygen diffusion for dislocations and for bulk are surprisingly similar, with $\Delta H_D^{\mathrm{dis},r=1\ \mathrm{nm}} = (2.95 \pm 0.21)$ eV and $\Delta H_D^{\mathrm{b}} = (2.67 \pm 0.13)$ eV. The effect of varying $r$ has only a small effect on the activation enthalpy $\Delta H_D^{\mathrm{dis}}$ (see Table 1).

Comparing, first, our activation enthalpy for bulk diffusion of oxygen in $\mathrm{La_{0.8}Sr_{0.2}MnO_{3+\delta}}$ with literature values reported for ceramics,[7,8] single grains in a ceramic[9] and thin films,[10,11] we find that our value of $\Delta H_D^{\mathrm{b}} = (2.67 \pm 0.13)$ eV lies fairly centrally within the range of 2.3 eV to 3.2 eV (see Table 1). In addition, our values of $D_{\mathrm{O}}^{*,\mathrm{b}}$ agree very well with reported data for ceramics[8,9] and thin films.[14] In this way, we establish that our bulk diffusion data constitute a firm basis for the subsequent analysis. Turning, then, to $D_{\mathrm{O}}^{*,\mathrm{dis}}$, we find but a single data point in the literature with which we can compare our data, and this was obtained for $\mathrm{La_{0.8}Sr_{0.2}MnO_3}$ thin films on $\mathrm{LaAlO_3}$ by Navickas et al.[14] with the assumption of $r = 1$ nm. Their value is more than one order of magnitude higher than ours, and this dif-

Table 1: Activation enthalpy for oxygen tracer diffusion $\Delta H_D$ in $La_{0.8}Sr_{0.2}MnO_{3+\delta}$. The upper section lists values obtained for the bulk phase, $\Delta H_D^{\mathrm{b}}$. The lower section summarizes results for the dislocations, $\Delta H_D^{\mathrm{dis,r}}$, obtained in this study for different assumed radii $r$ within which faster diffusion occurs.

| | $\Delta H_D$ [eV] |
|---|---|
| | bulk |
| This study | $2.67 \pm 0.13$ |
| Yasuda et al.[7] | $3.07 \pm 0.20$ |
| De Souza et al.[8] | $2.80 \pm 0.13$ |
| Fearn et al.[9] | $3.18 \pm 0.25$ |
| Navickas et al.[11] | $2.56 \pm 0.20$ |
| Saranya et al.[10] | $2.30 \pm 0.16$ |
| | dislocations |
| This study with: | |
| $r = 0.5$ nm | $3.06 \pm 0.21$ |
| $r = 1.0$ nm | $2.95 \pm 0.21$ |
| $r = 1.5$ nm | $2.86 \pm 0.20$ |

ference may be due to the use of rather thin films by Navickas et al.[14], or it may be due to the type of dislocations being different or to the chemistry of the dislocation cores being different.[13,23]

We move now to the results obtained by MD simulations. It is important to note that the initial structures of dislocations that we generated (see Computational) were not stable in the simulations at finite temperatures. Attributing this behavior to the charge of the cores, positively charged $(La^{3+}/Sr^{2+})O^{2-}$ and negatively charged $Mn^{3.2+}(O^{2-})_2$, we modified the compositions to produce neutral cores, $Sr^{2+}O^{2-}$ and $Mn^{4+}(O^{2-})_2$, and found that these compositional changes yielded stable dislocation core structures [see Figure 5(a)]. Introducing oxygen vacancies to the dislocation cores[37,57] or to the bulk regions, and monitoring the mean-squared-displacement of the oxide ions, $\langle r_{\mathrm{O}}^2 \rangle$, over an MD simulation, we observed that for both dislocation and bulk regions [Figure 5(b) and (c)] the evolution as a function of time was similar for all three directions of the simulation cell at two temperatures: $\langle r_{\mathrm{O}}^2 \rangle_z \approx \langle r_{\mathrm{O}}^2 \rangle_x \approx \langle r_{\mathrm{O}}^2 \rangle_y$. If preferential oxygen diffusion along the dislocation cores had occurred, we would have observed $\langle r_{\mathrm{O}}^2 \rangle_z \gg \langle r_{\mathrm{O}}^2 \rangle_x \approx \langle r_{\mathrm{O}}^2 \rangle_y$.

From the MD simulations we extracted the trajectories of successful oxide-ion jumps. We observed that at the beginning of the simulations a few vacancies leave the dislocation cores, and that during the simulations some oxide ions jump into the remaining vacancies along $\langle 110 \rangle$ directions in a zig-zag manner in and out of the cores ($\langle 110 \rangle$ constituting the jump directions for oxide-ion migration in the bulk). The migration barriers, however, are evidently similar to those in the bulk, since the $\langle r_{\mathrm{O}}^2 \rangle$ values did not deviate from one another substantially. No jumps directly along the cores were detected, despite the high site fraction of oxygen vacancies. That is, although sites are available for oxide-ion migration, the barriers are evidently too high to allow diffusion along the core to take place.

## 2.1 Discussion

Dislocations are widely termed fast diffusion paths. Strictly speaking, they should be termed faster diffusion paths, since their presence only becomes apparent in a diffusion experiment when diffusion along them, however fast or slow it is, is faster than in the bulk. Fast(er) diffusion along extended defects is not absolute, but relative. Consequently, the key quantities to consider are not absolute, but relative: the ratio of the activation enthalpies and the ratio of the diffusion coefficients.

One major result of this study, therefore, is the combination of $\Delta H_D^{\mathrm{dis}}/\Delta H_D^{\mathrm{b}} = (1.12 \pm 0.13)$ and $D_{\mathrm{O}}^{*,\mathrm{dis}}/D_{\mathrm{O}}^{*,\mathrm{b}} = 10^{2.25 \pm 0.09}$. This combination argues strongly against diffusion occurring along the cores and for diffusion occurring predominately within space-charge tubes. In the standard explanation of fast diffusion along dislocations (derived from work on metals), it is the lower activation enthalpy of diffusion that is responsible for the higher rate of diffusion.[58,59] If we start with our $D_{\mathrm{O}}^{*,\mathrm{b}}$ data and modify only the activation enthalpy, we would have to use $\Delta H_D^{\mathrm{dis}} \approx 2.25$ eV in order to achieve $D_{\mathrm{O}}^{*,\mathrm{dis}}/D_{\mathrm{O}}^{*,\mathrm{b}} = 10^{2.25 \pm 0.09}$.

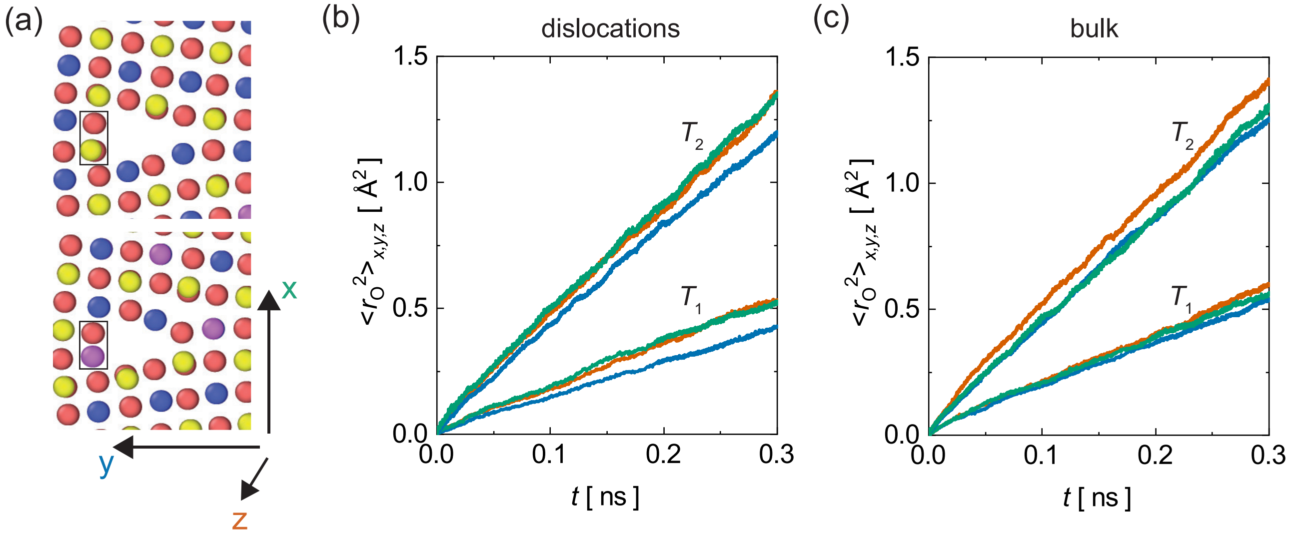

Figure 5: MD simulations of $\mathbf{b} = [010]$, $\mathbf{l} = [001]$ dislocations in $La_{0.8}Sr_{0.2}MnO_3$. (a) Sections of the simulation cell showing two different types of dislocation core, $MnO_2$-type (top) and SrO-type (bottom), indicated by the black boxes [La (blue), Sr (purple), Mn (yellow), O (red)]. Mean-squared-displacements of oxide ions along the $x$, $y$ and $z$ directions (colors according to (a)) of the simulation cell as a function of time at two different temperatures ($T_2 = 2500$ K, $T_1 = 2000$ K) for oxygen vacancies placed at the cores (b) and in the bulk (c).

Since the observed activation enthalpy is much higher, $\Delta H_D^{\mathrm{dis}} = (2.95 \pm 0.21)$ eV, this inconsistency suggests that the standard explanation — diffusion along cores — is highly unlikely. The space-charge tube explanation would avoid this inconsistency by augmenting $D_{\mathrm{O}}^{*,\mathrm{b}}$ by a term that reflects the accumulation of oxygen vacancies in the space-charge tube, that is, a term proportional to $\exp[2e\Phi_0(T)/k_{\mathrm{B}}T]$,[60] with $2e$ as the charge of the oxygen vacancies and $\Phi_0(T)$ as the temperature-dependent space-charge potential.

Indeed, a second major result is that the ratio of the activation enthalpies, $\Delta H_D^{\mathrm{dis}}/\Delta H_D^{\mathrm{b}} = (1.12 \pm 0.13)$, is equal to or higher than unity. A ratio substantially lower than unity would be expected if dislocation cores provide the predominant path for diffusion. In fact, for grain boundaries in oxides with dilute solutions of point defects it has been demonstrated[60] that diffusion along space-charge layers can give rise to $\Delta H_D^{\mathrm{gb}}/\Delta H_D^{\mathrm{b}}$ up to, but not higher than, unity [depending on the specific behavior of $\Phi_0(T)$]. Since fundamentally different behavior is not expected for $\Phi_0(T)$ at dislocations, it appears that $\Delta H_D^{\mathrm{dis}}/\Delta H_D^{\mathrm{b}} \leq 1$ is physically reasonable; effects arising from defect interactions between the high concentration of charge carriers in $La_{0.8}Sr_{0.2}MnO_{3+\delta}$ may be expected, though, to generate some differences (see below). Hence, on this basis, faster diffusion of oxygen along dislocations in $La_{0.8}Sr_{0.2}MnO_{3+\delta}$ is a space-charge phenomenon.

Let us examine two more complicated possibilities. Since the ratio of the diffusion coefficients is approximately constant, a higher pre-exponential factor for the dislocation case would account for the observed experimental data. The increase required, of over 5 $k_{\mathrm{B}}$, does not seem physically impossible, but it does seem extraordinary that the activation entropy of migration would be altered, but not the activation enthalpy. More importantly, an increased activation entropy would be apparent in the MD simulations, and this was not the case: vacancy diffusion was essentially unaffected. Thus this possibility can be safely excluded.

The second complicated possibility concerns altered oxygen-vacancy concentrations in the core. Since $\Delta H_D$ can be considered to be the sum of two terms, $\Delta H_D = \Delta H_{\mathrm{mig,v}} + \Delta H_{\mathrm{gen,v}}$ (with $\Delta H_{\mathrm{mig,v}}$ as the activation enthalpy of vacancy migration and $\Delta H_{\mathrm{gen,v}}$ as the enthalpy of vacancy generation, which charac-

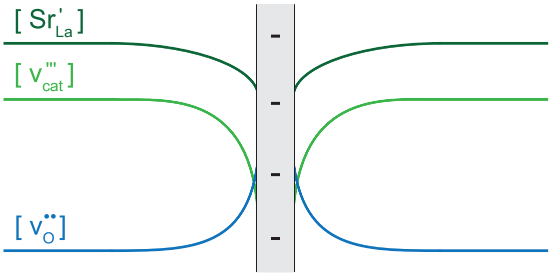

Figure 6: Possible scenario to explain fast diffusion along dislocations in $\mathrm{La}_{0.8}\mathrm{Sr}_{0.2}\mathrm{MnO}_{3+\delta}$ caused by a space-charge tube. Shown are selected charge-carrier concentrations on a log scale around a dislocation core.

terizes the change in vacancy concentration with temperature), one could claim that a decrease in $\Delta H_{\mathrm{mig,v}}$ could be (over-)compensated by an increase in $\Delta H_{\mathrm{gen,v}}$, giving in total an unchanged or even higher sum. The latter requires, however, that the defect thermodynamics of oxygen vacancies in the core differ to those in the bulk, and this then demands[40,42,61,62] that the possibility of charged dislocations and space-charge zones is taken into account. Furthermore, a lower value of $\Delta H_{\mathrm{mig,v}}$ can be discounted, since our MD simulations of oxygen tracer diffusion (Figure 5) indicated oxide-ion migration along oxygen-deficient dislocation cores was not faster than in the bulk.

For oxygen diffusion to be accelerated within space-charge tubes around dislocations in $\mathrm{La}_{0.8}\mathrm{Sr}_{0.2}\mathrm{MnO}_{3+\delta}$, oxygen vacancies — the point defects responsible for oxygen diffusion — have to be accumulated in the space-charge tubes. In the extensively studied perovskite system of acceptor-doped $\mathrm{SrTiO}_3$, oxygen vacancies are depleted in the space-charge tubes around dislocations.[1,37,52,62–67] The depletion arises from oxygen vacancies re-distributing from bulk to core in response to their Gibbs formation energy being lower in the core,[23,61,62] and in this way, giving the core a positive charge. This depletion results in oxygen transport being hindered by dislocation arrays.[52,63,64] To explain why dislocations in $\mathrm{La}_{0.8}\mathrm{Sr}_{0.2}\mathrm{MnO}_{3+\delta}$ behave differently, we require a different scenario, and the simplest is sketched in Figure 6. We assume that the dislocations cores in $\mathrm{La}_{0.8}\mathrm{Sr}_{0.2}\mathrm{MnO}_{3+\delta}$ are negatively charged, as this results in charge carriers with positive effective charge (oxygen vacancies) being accumulated and those with negative effective charge (acceptor dopant cations and cation vacancies) being depleted. The origin of the negative core charge is unclear, but on account of the high concentration of cation vacancies present in $\mathrm{La}_{0.8}\mathrm{Sr}_{0.2}\mathrm{MnO}_{3+\delta}$,[15–20] we tentatively propose that the charge comes from cation vacancies segregating from bulk to the dislocation cores. Quantitative calculations of charge-carrier profiles around a dislocation are outside the scope of this study, since a Poisson–Cahn approach[39,40,42] is required for this concentrated solution of defects, and this in turn requires an improved defect-chemical model for the bulk defects chemistry. A Poisson–Cahn approach is interesting because it may conceivably produce $\Delta H_D^{\mathrm{dis}}/\Delta H_D^{\mathrm{b}} > 1$.

Looking at Figure 6, we recognise an interesting additional effect that could follow from the behavior of cation vacancies. Since such species strongly inhibit the diffusion of oxygen vacancies,[21] their depletion within a space-charge tube means that the diffusivity of oxygen vacancies can no longer be taken as constant within a space-charge tube but will increase towards the core. Such effects may also conceivably produce $\Delta H_D^{\mathrm{dis}}/\Delta H_D^{\mathrm{b}} > 1$.

The increase in oxygen diffusivity along dislocations is relatively modest, at least for these dislocations. This means that very high dislocation densities ($\sim 10^{12.5}$ $\mathrm{cm}^{-2}$) are needed to increase the overall rate of oxygen diffusion through an LSMO thin film by a factor of 20 at $T = 923$ K, for example. Nevertheless, there is the possibility of altering the dislocations' nature and chemistry in order to modify the space-charge tubes. It may thus be possible to achieve the same increase at much lower dislocation densities, or much higher increases at the same dislocation density.

The presence of space-charge zones at dislocations in $\mathrm{La}_{0.8}\mathrm{Sr}_{0.2}\mathrm{MnO}_{3+\delta}$ implies that other extended defects, such as surfaces, grain boundaries and hetero-interfaces, will also have space-charge zones present. Indeed, studies of faster grain-boundary diffusion of oxygen in $\mathrm{La}_{0.8}\mathrm{Sr}_{0.2}\mathrm{MnO}_{3+\delta}$ yield relatively high values of $\Delta H_D^{\mathrm{gb}}/\Delta H_D^{\mathrm{b}}$, namely of $(1.17 \pm 0.07)$[8], (0.84)[10] and (1.31)[11]. Perhaps the system for which there are the most consequences is porous SOFC electrodes. Modeling such systems[68–70] will need to include space-charge effects on oxygen incorporation reaction from the gas phase into the oxide, the possibility of faster oxygen diffusion just below the surface within an accumulation space-charge layer, which would extend the active regions beyond the three-phase boundary of gas|electrode|electrolyte; and the transfer of oxide ions across the two-phase boundary between electrode and electrolyte.[71–73]

## 3 Concluding remarks

We combined a variety of experimental and computational methods to study the phenomenon of accelerated oxygen diffusion along dislocations in $La_{0.8}Sr_{0.2}MnO_{3+\delta}$. We concluded that this phenomenon cannot be explained by a lower barrier for oxide-ion migration along the cores. Rather, the presence of space-charge tubes enveloping the dislocations provides a consistent and comprehensive model of the observed behavior by explaining why $D_{\mathrm{O}}^{*,\mathrm{dis}}/D_{\mathrm{O}}^{*,\mathrm{b}} = 10^{2.25\pm0.09}$ is not inconsistent with $\Delta H_D^{\mathrm{dis}}/\Delta H_D^{\mathrm{b}} = (1.12 \pm 0.13)$ and by explaining the high value of $\Delta H_D^{\mathrm{dis}}/\Delta H_D^{\mathrm{b}} = (1.12 \pm 0.13)$. We suggested that cation vacancies are responsible for generating negatively charged dislocations and positive space-charge tubes in which oxygen vacancies are strongly accumulated. We also suggested that the behavior found here for dislocations is applied to other extended defects, such as surfaces, grain boundaries and interfaces with other oxides.

## 4 Methods Section

*Experimental*:
$La_{0.8}Sr_{0.2}MnO_3$ thin films were grown by pulsed laser deposition (PLD) on single-crystalline (001)-oriented STO substrates. The substrates (Shinkosha, Yokohama, Japan) were first treated in buffered HF for 150 s and then annealed at 950 °C for 2 h in synthetic air in order to achieve a smooth, $TiO_2$-terminated surface.[74]

Ablation of an $La_{0.8}Sr_{0.2}MnO_3$ ceramic target (Toshima Manufacturing, Higashimatsuyama, Japan) employed a pulsed KrF excimer laser (248 nm wavelength) with a laser frequency of 5 Hz, a laser fluence of 2.8 mJ $\mathrm{mm}^{-2}$ and a laser spot size on the target of 1.2 $\mathrm{mm}^2$. The target-to-substrate distance was 55 mm, the substrate was held at 850 °C through a resistive heater and the total pressure in the chamber was 0.24 mbar $O_2$. The growth was monitored in situ by reflection high-energy electron diffraction (RHEED). After growth a sample was cooled at 10 °C $\mathrm{min}^{-1}$ to room temperature in around 200 mbar $O_2$. Subsequently, films were given an oxidative treatment at 700 °C in synthetic air for 3 h.

After the oxidative treatment, samples were characterized by means of atom force microscopy (AFM; Cypher, OxfordInstruments Asylum Research, Santa Barbara, USA) and X-Ray diffraction (XRD;D8 Discover, BrukerAXS, Karlsruhe, Germany) with a monochromatic $K_{\alpha 1}$ X-ray beam. Electron diffraction and transmission electron microscopy (TEM) imaging were performed on a FEI Tecnai F20 at 200 kV. A TEM specimen was cut by focused ion beam (FIB) milling on an FEI Strata400 system with a $Ga^+$ beam.

$^{18}O/^{16}O$ exchange experiments were performed according to the standard procedure.[3,44] A sample was first annealed in oxygen of normal isotopic abundance at the temperature $T$ of interest and at $p\mathrm{O}_2 =$ 200 mbar for a duration of approximately ten times that of the subsequent isotope exchange anneal. The sample was then quenched to room temperature and subsequently exposed to $^{18}O$-enriched oxygen gas for a time $t$ at temperature $T$ and at $p\mathrm{O}_2 = 200$ mbar (see SI, Table S1 for details). Isotope profiles in the exchanged samples were measured by time-of-flight secondary ion mass spectrometry (ToF-SIMS) on a ToF-SIMS IV machine fitted with a ToF-SIMS.5 analyzer (IONTOF, Münster, Germany). Secondary ions for ToF analysis were generated by raster scanning a beam of 25 keV $Ga^+$ over 80 $\mu$m × 80 $\mu$m. Sputter etching of the surface was achieved by raster scanning 1 keV $Cs^+$ over 300 $\mu$m × 300 $\mu$m. Negative secondary ions were recorded with a ToF cycle time of 50 $\mu$s. Additionally, a beam of low-energy electrons was used for charge compensation. The pressure within the chamber was below $2 \cdot 10^{-9}$ mbar during this analysis. Crater depths were determined post-analysis by interference microscopy.

*Computational*:
Molecular dynamics (MD) simulations, based on the Born model of ionic solids, were carried out with periodic boundary conditions by means of the Lammps code.[75] The set of empirical pair potentials derived by Islam et al.[76] were used (with a cut-off of 12 Å). Simulations were performed in the $NpT$ ensemble with constant particle number $N$ at various temperatures in the range of $2000 \leq T$ [K] $\leq 3000$ and a pressure of $p = 0$. The simulation cell consisted of two anti-parallel 6° symmetrically tilted grains, ten unit cells thick, and was originally created for cubic STO.[57] It was adapted, first to $LaMnO_3$, by changing the composition and the cell dimensions, and then to $La_{0.8}Sr_{0.2}MnO_3$, by substituting at random 20% of $La^{3+}$ with $Sr^{2+}$ and compensating the excess charge by increasing the charge of all Mn ions to +3.2. The resultant cell has two periodic arrays of edge dislocations, of Burgers vector $\mathbf{b} = [010]$ and line vector $\mathbf{l} = [001]$, alternating between a positively charged (La/Sr)O-type core and a negatively charged $MnO_2$-type core. In order for oxygen diffusion to occur, oxide ions were deleted either from the dislocations or from the bulk region between them, the additional charge being compensated by a uniform background charge. During performed simulations the cell displayed a cubic bulk phase (SI, Figure S5).

**Supporting Information**
Supporting Information is available.

**Acknowledgements**
Funding from German Research Foundation (DFG) from project DE 2854/12-1 and from the collaborative research center SFB917 "Nanoswitches" is acknowledged. Simulations were performed with computing resources granted by RWTH Aachen University under project rwth0383 and rwth0737. L. Pasanisi is gratefully acknowledged for the support with the X-ray diffraction analysis.

## References

[1] V. Metlenko, A. H. Ramadan, F. Gunkel, H. Du, H. Schraknepper, S. Hoffmann-Eifert, R. Dittmann, R. Waser, R. A. De Souza, *Nanoscale* **2014**, *6*, 12864.

[2] R. A. De Souza, *J. Mater. Chem. A* **2017**, *5*, 20334.

[3] S. Carter, A. Selcuk, R. J. Chater, J. Kajda, J. A. Kilner, B. C. H. Steele, *Solid State Ionics* **1992**, *53-56*, 597.

[4] R. A. De Souza, J. A. Kilner, *Solid State Ionics* **1998**, *106*, 175.

[5] I. Yasuda, M. Hishinuma, *J. Solid State Chem.* **1996**, *123*, 382.

[6] A. V. Berenov, J. L. MacManus-Driscoll, J. A. Kilner, *Solid State Ionics* **1999**, *122*, 41.

[7] I. Yasuda, K. Ogasawara, M. Hishinuma, T. Kawada, M. Dokiya, *Solid State Ionics* **1996**, *86-88*, 1197.

[8] R. A. De Souza, J. A. Kilner, J. F. Walker, *Mater. Lett.* **2000**, *43*, 43.

[9] S. Fearn, J. C. H. Rossiny, J. A. Kilner, J. R. G. Evans, *Solid State Ionics* **2012**, *211*, 51.

[10] A. M. Saranya, D. Pla, A. Morata, A. Cavallaro, J. Canales-Vázquez, J. A. Kilner, M. Burriel, A. Tarancõn, *Adv. Energy Mater.* **2015**, *5*, 1500377.

[11] E. Navickas, T. M. Huber, Y. Chen, W. Hetaba, G. Holzlechner, G. Rupp, M. Stöger-Pollach, G. Friedbacher, H. Hutter, B. Yildiz, J. Fleig, *Phys. Chem. Chem. Phys.* **2015**, *17*, 7659.

[12] F. Chiabrera, A. Morata, M. Pacios, A. Tarancón, *Solid State Ionics* **2017**, *299*, 70.

[13] F. Chiabrera, I. Garbayo, L. López-Conesa, G. Martín, A. Ruiz-Caridad, M. Walls, L. Ruiz-González, A. Kordatos, M. Núñez, A. Morata, S. Estradé, A. Chroneos, F. Peiró, A. Tarancón, *Adv. Mater.* **2019**, *31*, 1.

[14] E. Navickas, Y. Chen, Q. Lu, W. Wallisch, T. M. Huber, J. Bernardi, M. Stöger-Pollach, G. Friedbacher, H. Hutter, B. Yildiz, J. Fleig, *ACS Nano* **2017**, *11*, 11475.

[15] B. Tofield, W. Scott, *J. Solid State Chem.* **1974**, *10*, 183.

[16] J. Mizusaki, H. Tagawa, K. Naraya, T. Sasamoto, *Solid State Ionics* **1991**, *49*, 111.

[17] J. Mizusaki, N. Mori, H. Takai, Y. Yonemura, H. Minamiue, H. Tagawa, M. Dokiya, H. Inaba, K. Naraya, T. Sasamoto, T. Hashimoto, *Solid State Ionics* **2000**, *129*, 163.

[18] F. W. Poulsen, *Solid State Ionics* **2000**, *129*, 145.

[19] D. S. Mebane, Y. Liu, M. Liu, *Solid State Ionics* **2008**, *178*, 1950.

[20] Y. L. Lee, D. Morgan, *Phys. Chem. Chem. Phys.* **2012**, *14*, 290.

[21] J. M. Börgers, R. A. De Souza, *Phys. Chem. Chem. Phys.* **2020**, *22*, 14329.

[22] J. M. Polfus, B. Yildiz, H. L. Tuller, *Phys. Chem. Chem. Phys.* **2018**, *20*, 19142.

[23] R. A. De Souza, *Curr. Opin. Solid State Mater. Sci.* **2021**, *25*, 100923.

[24] S. J. Skinner, *Int. J. Inorg. Mater.* **2001**, *3*, 113.

[25] N. Q. Minh, *J. Am. Ceram. Soc.* **1993**, *76*, 563.

[26] S. B. Adler, *Chem. Rev.* **2004**, *104*, 4791.

[27] B. C. H. Steele, *Solid State Ionics* **1996**, *86-88*, 1223.

[28] Y. Wang, K.-M. Kang, M. Kim, H.-S. Lee, R. Waser, D. Wouters, R. Dittmann, J. J. Yang, H.-H. Park, *Mater. Today* **2019**, *28*, 63.

[29] J. C. Gonzalez-Rosillo, R. Ortega-Hernandez, J. Jareño-Cerulla, E. Miranda, J. Suñe, X. Granados, X. Obradors, A. Palau, T. Puig, *J. Electroceram.* **2017**, *39*, 185.

[30] J. C. Gonzalez-Rosillo, R. Ortega-Hernandez, B. Arndt, M. Coll, R. Dittmann, X. Obradors, A. Palau, J. Suñe, T. Puig, *Adv. Electron. Mater.* **2019**, *1800629*, 1.

[31] L. Yao, S. Inkinen, S. Van Dijken, *Nat. Commun.* **2017**, *8*, 1.

[32] N. Jedrecy, V. Jagtap, C. Hebert, L. Becerra, D. Hrabovsky, A. Barbier, X. Portier, *Adv. Electron. Mater.* **2021**, *7*, 2000723.

[33] B. Meunier, D. Pla, R. Rodriguez-Lamas, M. Boudard, O. Chaix-Pluchery, E. Martinez, N. Chevalier, C. Jiménez, M. Burriel, O. Renault, *ACS Appl. Electron. Mater.* **2019**, *1*, 675.

[34] L. Yao, S. Inkinen, H. P. Komsa, S. van Dijken, *Small* **2021**, *17*, 2006273.

[35] Y. K. Ho, P. L. Pratt, *Radiat. Eff.* **1983**, *75*, 183.

[36] A. Atkinson, *Solid State Ionics* **1984**, *12*, 309.

[37] S. P. Waldow, R. A. De Souza, *ACS Appl. Mater. Interfaces* **2016**, *8*, 12246.

[38] D. Marrocchelli, L. Sun, B. Yildiz, *J. Am. Chem. Soc.* **2015**, *137*, 4735.

[39] D. S. Mebane, *Comput. Mater. Sci.* **2015**, *103*, 231.

[40] X. Tong, D. S. Mebane, R. A. De Souza, *J. Am. Ceram. Soc.* **2020**, *103*, 5.

[41] P. Fielitz, G. Borchardt, *Solid State Ionics* **2001**, *144*, 71.

[42] A. F. Zurhelle, X. Tong, A. Klein, D. S. Mebane, R. A. De Souza, *Angew. Chem. Intl. Ed.* **2017**, *56*, 14516.

[43] R. A. De Souza, J. Zehnpfenning, M. Martin, J. Maier, *Solid State Ionics* **2005**, *176*, 1465.

[44] R. A. De Souza, R. J. Chater, *Solid State Ionics* **2005**, *176*, 1915.

[45] R. A. De Souza, M. Martin, *MRS Bulletin* **2009**, *34*, 907.

[46] J. A. Kilner, S. J. Skinner, H. H. Brongersma, *J. Solid State Electrochem.* **2011**, *15*, 861.

[47] A. D. Le Claire, A. Rabinovitch, *J. Phys. C Solid State Phys.* **1981**, *14*, 3863.

[48] M. Gaudon, C. Laberty-Robert, F. Ansart, P. Stevens, A. Rousset, *Solid State Sci.* **2002**, *4*, 125.

[49] T. Grande, J. R. Tolchard, S. M. Selbach, *Chem. Mater.* **2012**, *24*, 338.

[50] O. Lebedev, G. Van Tendeloo, S. Amelinckx, *Int. J. Inorg. Mater.* **2001**, *3*, 1331.

[51] L. Yan, P. A. Salvador, *ACS Appl. Mater. Interf.* **2012**, *4*, 2541.

[52] K. K. Adepalli, J. Yang, J. Maier, H. L. Tuller, B. Yildiz, *Adv. Funct. Mater.* **2017**, *27*, 1700243.

[53] L. Porz, T. Frömling, A. Nakamura, N. Li, R. Maruyama, K. Matsunaga, P. Gao, H. Simons, C. Dietz, M. Rohnke, J. Janek, J. Rödel, *ACS Nano* https://doi.org/10.1021/acsnano.0c04491.

[54] X. Fang, L. Porz, K. Ding, A. Nakamura, *Crystals* **2020**, *10*, 1.

[55] H. Schraknepper, C. Bäumer, R. Dittmann, R. A. De Souza, *Phys. Chem. Chem. Phys* **2015**, *17*, 1060.

[56] Y.-C. Chung, B. J. Wuensch, *J. Appl. Phys.* **1996**, *79*, 8323.

[57] A. H. Ramadan, R. A. De Souza, *Acta Mater.* **2016**, *118*, 286.

[58] R. W. Balluffi, *Phys. Status Solidi* **1970**, *42*, 11.

[59] J. Mimkes, *Thin Solid Films* **1975**, *25*, 221.

[60] J. P. Parras, R. A. De Souza, *Acta Mater.* **2020**, *195*, 383.

[61] P. C. McIntyre, *J. Am. Ceram. Soc.* **2000**, *83*, 1129.

[62] R. A. De Souza, *Phys. Chem. Chem. Phys.* **2009**, *11*, 9939.

[63] H. Schraknepper, T. E. Weirich, R. A. De Souza, *Phys. Chem. Chem. Phys.* **2018**, *20*, 15455.

[64] R. A. De Souza, J. Fleig, J. Maier, O. Kienzle, Z. Zhang, W. Sigle, M. Rühle, *J. Am. Ceram. Soc.* **2003**, *86*, 922.

[65] R. A. De Souza, J. Fleig, J. Maier, Z. Zhang, W. Sigle, M. Rühle, *J. Appl. Phys.* **2005**, *97*, 53502.

[66] Z. Zhang, W. Sigle, R. A. De Souza, W. Kurtz, J. Maier, M. Rühle, *Acta Mater.* **2005**, *53*, 5007.

[67] X. Guo, Z. Zhang, W. Sigle, E. Wachsman, R. Waser, *Appl. Phys. Lett.* **2005**, *87*, 1.

[68] J. D. Fehribach, R. O'Hayre, *SIAM J. Appl. Math.* **2009**, *70*, 510.

[69] M. Gong, R. S. Gemmen, D. S. Mebane, K. Gerdes, X. Liu, *J. Electrochem. Soc.* **2014**, *161*, F344.

[70] G. F. Brunello, W. K. Epting, J. de Silva, P. A. Salvador, S. Litster, H. O. Finklea, Y.-L. Lee, K. R. Gerdes, D. S. Mebane, *Phys. Chem. Chem. Phys.* **2017**, *19*, 25334.

[71] T. Horita, K. Yamaji, M. Ishikawa, N. Sakai, H. Yokokawa, T. Kawada, T. Kato, *J. Electrochem. Soc.* **1998**, *145*, 3196.

[72] T. Horita, K. Yamaji, N. Sakai, Y. Xiong, T. Kato, H. Yokokawa, T. Kawada, *J. Power Sources* **2002**, *106*, 224.

[73] T. M. Huber, M. Kubicek, A. K. Opitz, J. Fleig, *J. Electrochem. Soc.* **2014**, *162*, F229.

[74] G. Koster, B. L. Kropman, G. J. H. M. Rijnders, D. H. A. Blank, H. Rogalla, *Appl. Phys. Lett.* **1998**, *73*, 2920.

[75] S. Plimpton, *J. Comp. Phys.* **1995**, *117*, 1.

[76] M. Islam, M. Cherry, C. Catlow, *J. Solid State Chem.* **1996**, *124*, 230.

## Table of Contents

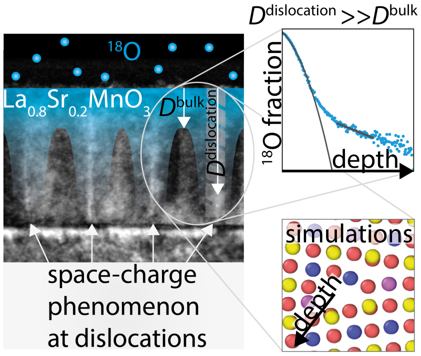

A judicious combination of experimental and computational methods is used to identify the origin of faster oxygen diffusion along dislocations in the perovskite-oxide (La,Sr)$MnO_{3+\delta}$. Taken together, the results from $^{18}O$ diffusion experiments and from molecular dynamics (MD) simulations indicate that faster diffusion cannot occur along the structural core of the dislocations, but rather along enveloping space-charge tubes.